Impact of the binder nature on the morphological change of sulfur electrodes upon cycling investigated by in situ characterization methods

Quentin Lemarié, Hassane Idrissi, Eric Maire, Pierre-Xavier Thivel, Fannie Alloin, Lionel Roue

Impact of the binder nature on the morphological change of sulfur electrodes upon cycling investigated by *in situ* characterization methods

Quentin Lemarié[a,b], Hassane Idrissi[b], Eric Maire[b], Pierre-Xavier Thivel[c], Fannie Alloin[c], Lionel Roué[a,*]

[a] *INRS- Énergie, Matériaux, Télécommunications, Varennes, Québec, J3X 1S2, Canada*

[b] *Université de Lyon, INSA-Lyon, MATEIS, CNRS UMR5510, F-69621 Villeurbanne, France*

[c] *Univ. Grenoble Alpes, Univ. Savoie Mont Blanc, CNRS, Grenoble INP, LEPMI, 38000 Grenoble, France*

** Corresponding author: roue@emt.inrs.ca (Lionel Roué)*

Abstract

The binder used in the formulation of sulfur electrodes for Li/S batteries plays a crucial role in their electrochemical performance. In the present study, the impact of using a polyelectrolyte binder (poly(diallyldimethylammonium) bis(trifluromethane sulfonyl)imide) on the morphological degradation of sulfur electrodes is evaluated by *in situ* dilatometry, acoustic emission (AE) and synchrotron X-ray tomography (XRT), and compared to more conventional binders (poly(vinylidene difluoride) (PVdF) and carboxymethyl cellulose (CMC)). The dilatometry study shows that during the initial sulfur dissolution process, the polyelectrolyte-based electrode displays a lower irreversible thickness contraction of ~16% compared to ~22% and ~31% for CMC and PVdF, respectively. This is confirmed by the XRT measurements showing a reduced thickness variation for the polyelectrolyte electrode compared to the CMC electrode. The same trend is found in the AE results, where a lower acoustic activity attributed to the rupture of the binder/carbon/sulfur network is detected during the 1st discharge plateau for the polyelectrolyte electrode. All these results confirm the major role of the binder for the Li/S system. Thanks to its multifunctionality, it impacts both the diffusion of the active material outside the electrode and the electrode integrity and therefore the conduction paths and accessible active surface for electrochemical processes.

Keywords: *lithium-sulfur battery; sulfur electrode binder; morphological degradation, X-ray tomography; acoustic emission; dilatometry*

1. Introduction

Due to the rarefaction of its core electrode materials and its inability to fully meet the constantly increasing requirements of electric vehicles (EV), the currently dominant lithium-ion technology needs to be replaced by a new generation of batteries [1]. The lithium-sulfur (Li/S) system stands as a promising technology. Its positive electrode active material (elemental sulfur) is both abundant and low cost, and provides a theoretical specific capacity of 1672 mAh g^{-1} (hence a theoretical energy density of 2567 Wh kg^{-1} for Li/S *versus* 387 Wh kg^{-1} for a typical graphite/$LiCoO_2$ system) [1]. However, the chemical and electrochemical reactions operating the charge transfer in the Li/S system involve the dissolution and precipitation of sulfur species, inducing major morphological changes of the positive electrode, and impacting the performance of the batteries [2].

Thus over the past few years, many published studies focused on improving the performance of Li/S batteries through optimizing the components of the positive electrode [3–5]. In particular, the binder plays a key role in maintaining the mechanical integrity of the electrode through cycling [5]. Conventional binders for Li-ion battery electrodes such as poly(vinylidene fluoride) (PVdF) [6] and poly(ethylene oxide) (PEO) [7] were initially used in sulfur-based electrodes. However, their mechanical strength is insufficient to withstand the huge volume change of the S electrodes during cycling in addition to suffering from swelling in ether-based electrolytes. Water-soluble binders, such as carboxymethylcellulose (CMC) [8] or polyacrylic acid (PAA) [9], are also popular binder materials for sulfur-based electrodes due to their functional groups (*e.g.* –COOH), which can form strong covalent bonds with the electrode materials. Crosslinked binders for further mechanical robustness, such as CMC with citric acid [10], were also evaluated, resulting in a better maintained electronic/physical connection among the sulfur composites. Some recent studies focus on using functional materials in order for the binder to actively participate to the confinement of

the soluble polysulfide species and/or to improve electron or ion transport [5,11–14]. For instance, cationic polyelectrolyte binders, such as poly(diallyldimethylammonium) bis(trifluromethane sulfonyl)imide (PDDA-TFSI) [14], are able to restrict the diffusion of soluble polysulfide species into the electrolyte thanks to preferential and strong electrostatic interactions of the polysulfide anions with the cationic polymer backbone. In addition, they are able to facilitate the lithium ion transport in the sulfur electrode through the reconfigurable network of anions associated with the cationic polymer backbone. As a result, high accessible capacity (up to ~8 mAh cm^{-2}) at high C-rates (up to 2 C) at a high areal sulfur loading (up to ~8 mg cm^{-2}) can be obtained [14].

The morphological variation of sulfur electrodes is usually investigated through *ex situ* scanning electron microscopy (SEM) observations performed after different periods of cycling. However, such *ex situ/post mortem* characterization methods do not give information on the dynamic of the morphological change of the sulfur electrodes upon cycling. For that purpose, *in situ* characterization techniques are required. In the present study, three different *in situ* characterization techniques are used, namely acoustic emission (AE), electrochemical dilatometry and synchrotron X-ray tomography.

The first one consists in measuring the acoustic signals emitted during the electrode cycling thanks to an AE sensor connected to the electrochemical cell. This method has been initially used to detect anomalies and failures (*e.g*. leakages and cracks) on large structures (*e.g*. bridges and pipe lines) and to characterize the degradation mechanism of various materials under mechanical, thermal or chemical stress. More recently, acoustic emission has been applied to electrode materials for Ni-MH [15], Li-ion [16] and Li-S batteries [17], mainly to monitor their mechanical degradation (*e.g*. cracking, collapsing) upon cycling.

The electrochemical dilatometry technique allows to measure the thickness variations of an electrode material undergoing electrochemical reactions through the use of a

displacement transducer integrated in the electrochemical cell. For instance, it has been used to characterize the expansion/contraction behavior of graphite [18] and Si anodes [19] for Li-ion batteries and more recently of a Li_2S/carbon cloth electrode for Li/S batteries [20].

In situ X-ray computed tomography (XRCT) is a powerful analytical tool to get a direct observation on the structural changes of battery electrodes upon cycling and to get crucial morphological parameters such as volume fraction, size distribution or connectivity of the different segmented phases inside the electrode. Using a synchrotron X-ray source also grants higher spatial and phase contrast resolutions and reduces acquisition times. This technique has been used to characterize various types of battery electrodes, such as $LiCoO_2$ [21], Si [22,23] Li metal [24] and sulfur electrodes [25–28].

The objective of the present study is to evaluate the ability of the *in situ* AE, dilatometry and synchrotron XRCT characterization techniques to study the influence of the binder nature (PVdF, CMC and PDDA-TFSI) on the morphological change of the electrode during the electrochemical processes. On the basis of these analyses, it is shown that the morphological change of the sulfur electrode is less marked with the PDDA-TFSI binder, confirming the efficiency of this cationic polyelectrolyte binder to enhance the mechanical strength of the sulfur based electrodes.

2. Experimental

2.1. Electrode preparation

The PDDA-TFSI binder was obtained by anionic exchange between PDDACl and LiTFSI as described in our previous work [28]. As-received sulfur (S) powder (-325 mesh, 99.5%, Alfa Aesar) was used as active material and carbon black (CB) (Super P, Timcal) as a conductive additive. The electrode composition was fixed to 70/20/10 wt% (S/CB/PDDA-TFSI). An aluminum foil (20 µm thick, MTI) was used as current collector. PVdF (Solef®

6020 grade, Solvay) and CMC (DS=0.9, Mw=700,000, Sigma-Aldrich) were also used as binder for comparison. Depending on the nature of their binder, the electrodes were labelled as PVdF, CMC and PDDA in this work.

A homogenous mixture of S and CB powders was obtained by manual grinding in an agate mortar for 15 minutes with a few drops of cyclohexane. The PDDA-TFSI and PVdF binders were dissolved in N-methyl-pyrrolidone (NMP) (anhydrous, 99.5%, Sigma-Aldrich) in order to obtain a 12 wt% binder solution. The CMC binder was dissolved in deionized water to obtain a 3 wt% binder solution.

The binder solution and the S+CB powder mixture were poured in a silicon nitride vial along with three silicon nitride milling balls. The slurry was mixed using a Fritsch Pulverisette 7 mixer at 500 rpm for 1 hour, forming a homogenized ink which was coated onto the Al current collector using a doctor-blade technique. The electrodes were then dried at 60°C for 24 hours in a vacuum oven before being cut into discs of various diameters depending on the experiment (see below) and stored in an argon-filled glove box. The areal sulfur loading of the electrodes was kept as constant as possible by tailoring the blade gap during the coating, with the loading of all electrodes being of 3±0.5 mg_{sulfur} cm^{-2}.

The morphology of the pristine electrodes was characterized by surface and cross-sectional SEM observations performed using a Tescan VEGA 3 microscope.

2.2. Electrochemical performance

Conventional CR2032 two-electrode coin cells were used for evaluating the electrochemical performance of the sulfur electrodes. They were assembled in an argon-filled glove box by stacking the sulfur electrode (1.2 cm diam.), a thick polyolefin non-woven tissue (Viledon®, Freudenberg) serving as electrolyte reservoir and separator, a polypropylene separator (Celgard® 2400) and a lithium metal disk (MTI, 1.4 cm diam.)

serving as counter electrode. A standard electrolyte for Li/S batteries was used, composed of 1 M LiTFSI and 0.1 M $LiNO_3$ additive (Aldrich) dissolved in a 1/1 volume ratio mixture of tetraethylene glycol dimethyl ether (TEGDME, 99%, Aldrich) and 1,3-dioxolane (DIOX, anhydrous, 99.8%, Aldrich). 150 µL of electrolyte was poured onto the sulfur electrode and the separators in order to completely soak the porosity of all the materials.

The electrochemical cycling experiments were performed on a BTS4000 (Neware) battery cycler. The cells were galvanostatically cycled between 1.5 and 3.0 V *vs*. Li/Li^+ at various C-rates ranging from C/50 to 1C. The values of the applied current were calculated based on the sulfur loading of each electrode and the theoretical capacity of sulfur (1672 mAh g^{-1}). The electrode capacities are expressed in mAh per g of sulfur.

2.3. Electrochemical dilatometry

An electrochemical dilatometer (ECD-2, El-CELL GmbH, Germany) was used to measure the thickness change of the sulfur electrodes during cycling. The dilatometry setup is schematized in **Fig. S1a**. The working electrode (1 cm diam.) and the lithium counter electrode are separated by a thick glass frit which is fixed in position. 2 mL of electrolyte were used in order to completely soak the glass frit. The height changes occurring at the working electrode during cycling are transmitted to the sensor unit and detected by a high-resolution displacement transducer. A slow cycling rate of C/50 was used, which was controlled by a VMP3 potentiostat/galvanostat (Bio-Logic). The dilatometric experiments were repeated at least 3 times for each electrode formulation. The thickness variation of the working electrode is expressed in relative change (%) of the initial thickness (excluding the Al substrate) of the electrode measured before cell assembly by using a digital micrometer (Mitutoyo). The initial thickness of the electrodes was typically around 60 µm for a loading of 3 mg_{sulfur} cm^{-2}.

2.4. Electrochemical acoustic emission

The AE signals were recorded using a nano 30 sensor (Mistras, operating frequency range 125-750 kHz) applied on the sulfur electrode side of the CR2032 coin cell, while a Katpon® polyimide film was placed in-between as a current insulator. The AE acquisition setup is schematized in **Fig. S1b**. The experiments were run at a slow cycling rate of C/50 and repeated at least 3 times per electrode formulation. The details of the AE acquisition parameters are described in our previous work [17].

2.5. In situ synchrotron X-ray tomography

In situ XRCT experiments were performed on the CMC and PDDA based electrodes using two different beamlines because the amount of beam time allocated on each beamline was too short to perform both experiments at the same place. Moreover, due to the limited beam time, XRCT experiment was not performed on the PVdF electrode.

The CMC electrode was studied at the PSICHÉ beamline at the SOLEIL facility (Gif-sur-Yvette, France), and the PDDA based electrode was studied at the ID11 beamline at the European Synchrotron Radiation Facility (ESRF) (Grenoble, France). In both cases, a two-electrode Swagelok cell, specifically designed for XRCT measurements, was used as schematized in **Fig. S1c**. The cell housing was made of perfluoroalkoxy alkane (PFA) polymer with a wall thickness reduced to 2.5 mm near the electrode to ensure a lower X-ray attenuation and better image quality. The diameter of the sulfur electrode was 2.5 mm. Both studies were done at a cycling rate of C/20, with the cell being set to open circuit potential (OCP) during the acquisition of the radiographs, which were conducted at regular intervals (typically, every 30 mins) during the 1st cycle. The OCP durations were ~5 and ~20 mins per XRCT acquisition step for the CMC and the PDDA electrodes, respectively.

For the XRCT experiment on the CMC based electrode, the synchrotron beam energy was set at 25 keV (λ = 0.0496 nm) using an X-ray mirror and Ag filters. The PyHST2 software [29] was used to reconstruct 3D tomographic volumes of $1331 \times 1331 \times 390$ µm^3 with an isotropic voxel size of 0.65 µm (spatial resolution of about 1.3 µm), *i.e.* in a so-called 'local tomography' mode. These dimensions were calibrated to cover the whole active height of the cell, from the current collector on the sulfur electrode side to the other one on the lithium metal electrode side. In order to facilitate the image analyses, the studied zone was cropped from the bottom of the sulfur electrode up to the separator, corresponding to an analyzed volume of $1331 \times 1331 \times 65$ µm^3.

For the XRCT experiment on the PDDA based electrode, the energy of the beam was set at 38 keV (λ = 0.0326 nm) and a beam size of 1×1 mm². The volume of the 3D reconstructions was of $1433 \times 1433 \times 490$ µm^3 with an isotropic voxel size of 0.7 µm (spatial resolution of about 1.4 µm), *i.e.* again in a local tomography mode. The dimensions of the analyzed volume was reduced to $1433 \times 1433 \times 70$ µm^3 to focus on the sulfur electrode.

In all the presented XRCT images, the grayscale levels correspond to the attenuation coefficient, therefore denser regions appear brighter. All image processing and quantitative analyses were performed using the Fiji software [30].

3. Results and discussion

3.1. Electrode morphology at the pristine state

Fig. 1a-f shows SEM images of the surface and cross-section of the PVdF, CMC and PDDA based electrodes at the pristine state. Sulfur particles/agglomerates with irregular shapes and various sizes, ranging from about 5 to 40 µm, are discernible on the micrographs. They appear well interconnected through the binder and homogenously covered with submicrometric CB particles, which are however not clearly visible on the images. The

global morphology of the electrode is rather similar for the different formulation. However, the sulfur agglomerates seem to be smaller for the PDDA electrode. Since the electrode morphology is dependent on the dispersion degree of the electrode ink, this may indicate a better dispersion of the sulfur particles during the ink preparation due to higher electrostatic repulsing effects, better flexibility and/or more stretched conformation of the cationic PDDA chains compared to the CMC and PVdF binders. To confirm the positive impact of the PDDA-TFSI binder on the ink properties, measurements such as the zeta potential of the sulfur particles and the sedimentation rate of the ink should be carried out as done with CMC binder in the literature [31].

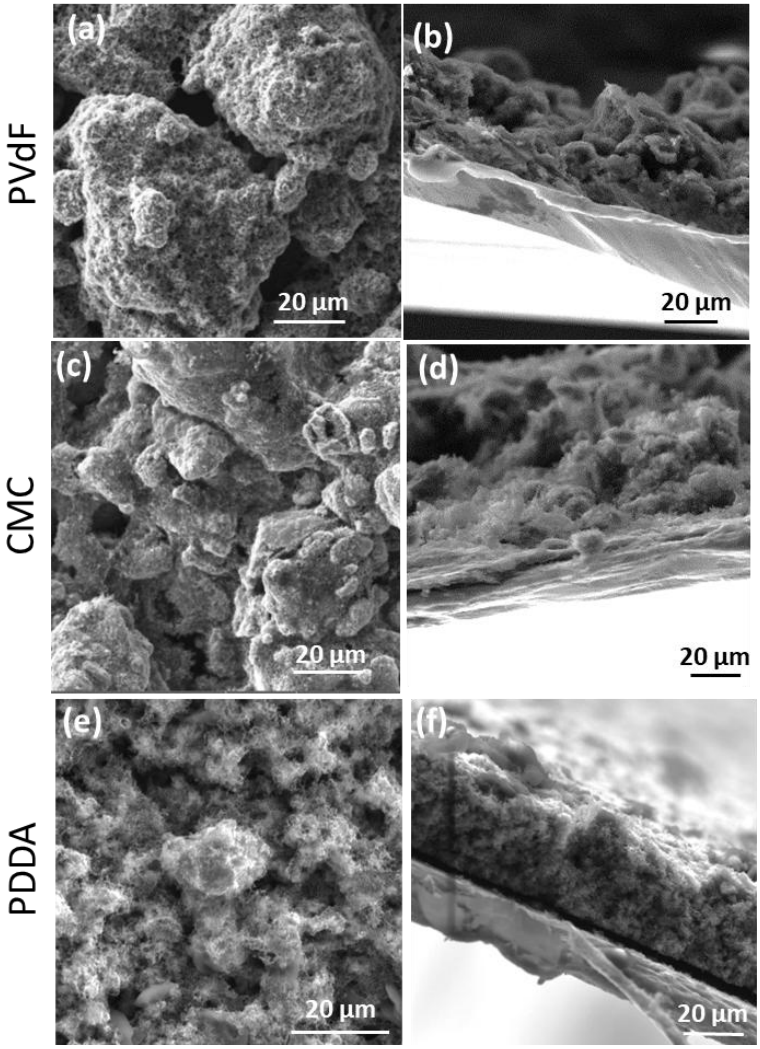

Figure 1. SEM micrographs of pristine (a, b) PVdF, (c, d) CMC and (e, f) PDDA-based electrode: (a, c. e) top view and (b, d, f) cross-section

3.2.Electrochemical performance

The cycling performance of the three different formulations (PVdF, CMC and PDDA) were tested and compared. **Fig. 2a** shows the evolution of their specific discharge capacity during up to ~60-100 cycles at C/50. As already stated in previous studies [17,32], PVdF and CMC formulations display overall similar performance, with an initial capacity around 650 mAh g^{-1}, quickly dropping during the first 5 to 15 cycles followed by a slower capacity decay to reach a discharge capacity around 250 mAh g^{-1} at the 50^{th} cycle. On the other hand, the PDDA formulation shows a much higher initial discharge capacity of around 1050 mAh g^{-1} with a reduced capacity loss after about 10 cycles, reaching a nearly stable value of 730 mAh g^{-1}. More precisely, a relative capacity decay of only 7% is observed between the 10^{th} and 50^{th} cycle for the PDDA electrode compared to 35% and 30% for the PVdF and CMC electrode, respectively.

The better capacity retention of the PDDA electrode is also highlighted in **Fig. 2b-d,** displaying the voltage profiles at the 1^{st}, 10^{th} and 50^{th} cycles of each formulation. At the 1^{st} cycle, the 1^{st} discharge plateau observed at about 2.4V is similar for all the electrodes and close to the theoretical value of 279 mAh g^{-1} for the lithiation of solid sulfur in soluble Li_2S_6 [33], meaning that initially the sulfur particles are almost fully accessible whatever the binder. In contrast, the 2^{nd} discharge plateau of the 1^{st} cycle situated at about 2.0V is much longer for the PDDA electrode. This can be attributed to the ability of the PDDA to restrict the diffusion of soluble polysulfide species into the electrolyte due to the strong electrostatic interactions of the lithium polysulfides with the cationic polymer backbone of the PDDA-TFSI binder [14] and thus a larger amount of Li_2S_2/Li_2S is likely to be formed on the positive electrode. It can also partially result from a better preservation of the PDDA electrode conductive network (lower electrode collapsing) after dissolution of the sulfur particles as suggested below from the *in situ* dilatometry, AE and XRCT experiments. Moreover, the

voltage hysteresis between the discharge and charge of the 2nd plateau is significantly lower for the PDDA electrode (*ca.* 160 mV *vs.* 210 and 270 mV for the CMC and PVdF electrode, respectively) reflecting lower polarization. This could be related to an easier lithium ion transport in the sulfur electrode thanks to the reconfigurable anionic network of the PDDA-TFSI binder [14] and/or an improvement of the electronic network associated with the higher mechanical strength of the electrode as discussed below. As the cycling progresses, a decrease on the 1st and 2nd discharge plateaus is observed but is much less marked for the PDDA formulation. At the 50th cycle, the value of the 1st plateau is of around 130 mAh g^{-1} for PDDA against merely 50 mAh g^{-1} for PVdF and CMC. This indicates that a larger amount of active material (S_8) is being dissolved (electroactive) at the 50th cycle of the PDDA electrode compared to the other two, hinting at a reduced loss of active material during the repeated dissolution/deposition cycles. This can be attributed to the ability of the PDDA binder to hold back part of the polysulfide species inside the electrode as previously discussed, as well as maintaining a more mechanically stable electrode through cycling. Finally, it can be noted that the potential of the 2nd discharge plateau of the PDDA electrode appears to be similar between the 1st and the 50th cycles, meaning that its polarization resistance does not increase with cycling. The decrease in capacity can here be attributed mainly to the loss of active material instead of contact failures.

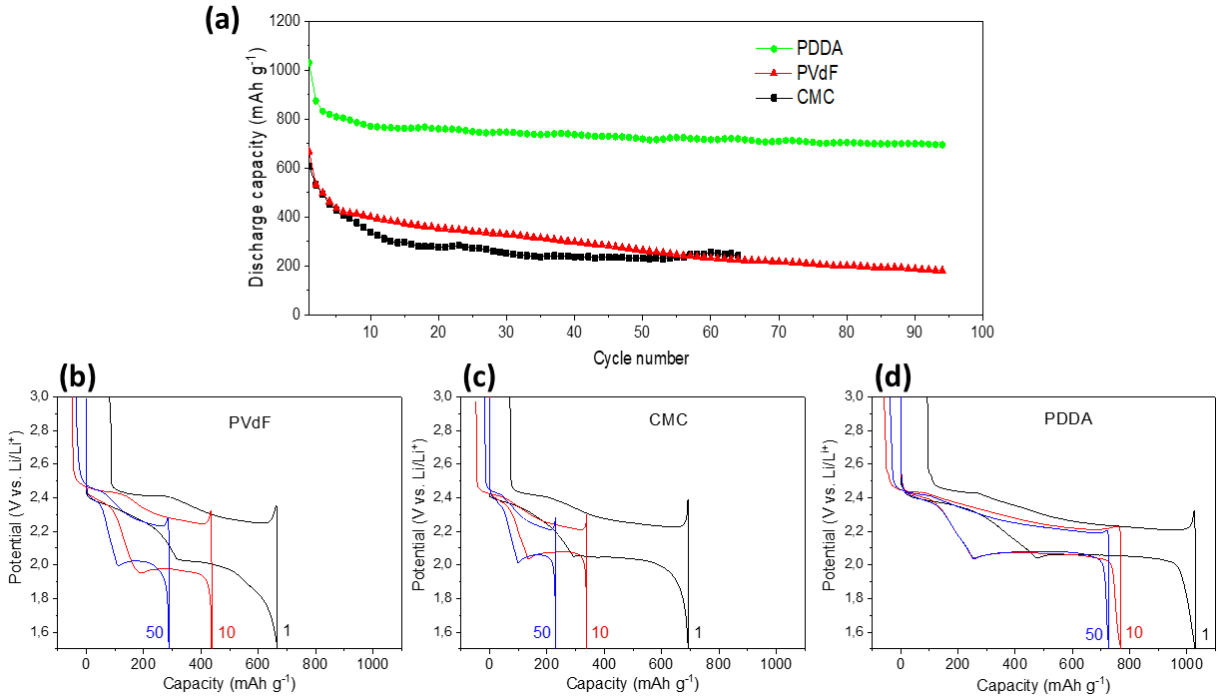

Figure 2. (a) Cycling performance of the PVdF, CMC and PDDA electrodes cycled at C/50 and voltage profiles at the 1st, 10th and 50th cycles for the (b) PVdF, (c) CMC and (d) PDDA electrodes.

The rate capabilities of the PVdF, CMC and PDDA electrodes are compared in **Fig. 3**. The electrodes have been cycled 5 times at C/50, C/20, C/10, C/5 and 1C successively, before being cycled 5 times at C/50 again. A better rate capability performance is observed with the PDDA electrode in accordance with its lower polarization as previously discussed. For instance, the PDDA electrode displays a discharge capacity of 380 mAh g^{-1} at 1C, hence 54% of its stabilized discharge capacity at C/20 whereas the PVdF and CMC electrodes display only a discharge capacity of 90 and 55 mAh g^{-1}, corresponding to 27 and 14% of their stabilized discharge capacity at C/20, respectively. On the voltage profiles at different C-rates, it is observed that the 2nd discharge plateau of both PVdF and CMC electrodes is quickly shifted below 2V at C/20 and C/10, while the 2nd plateau of the PDDA electrode remains around 2.05V. Then, at higher rates of C/5 and 1C, the PVdF and CMC electrode display a very steep 2nd plateau, almost indiscernible, while this plateau is still clearly marked on the PDDA electrode despite being shifted down to ~1.6V at 1C. These observations point

out that if the polarization increases along with the C-rate, as expected owing to ohmic drop, for all electrodes, the PDDA electrodes is less affected, because of the lower impedance of the cell. Additionally, it can be seen that when the electrodes are cycled again at C/50, their recovered charge capacity is much higher than their corresponding discharge capacity. It is related to the well-known shuttle reaction [2]. This reaction is likely to be favored by the formation of Li dendrites and the degradation of the SEI on the lithium metal negative electrode, which are accentuated at high areal current density according to the Sand's model [34–36]. Thus, at 1C cycling, corresponding to an areal anodic current density of ~3.5 mA cm^{-2}, severe dendrite growth and SEI cracking are likely to occur (especially for the PDDA electrode due its higher capacity at 1C inducing a longer Li plating time). This would imply a larger reactive interface between the lithium electrode and the electrolyte when cycled back at a slow C-rate of C/50, inducing more lithium polysulfide redox shuttle effect in the electrolyte, affecting the duration of the charge and the coulombic efficiency of the cell.

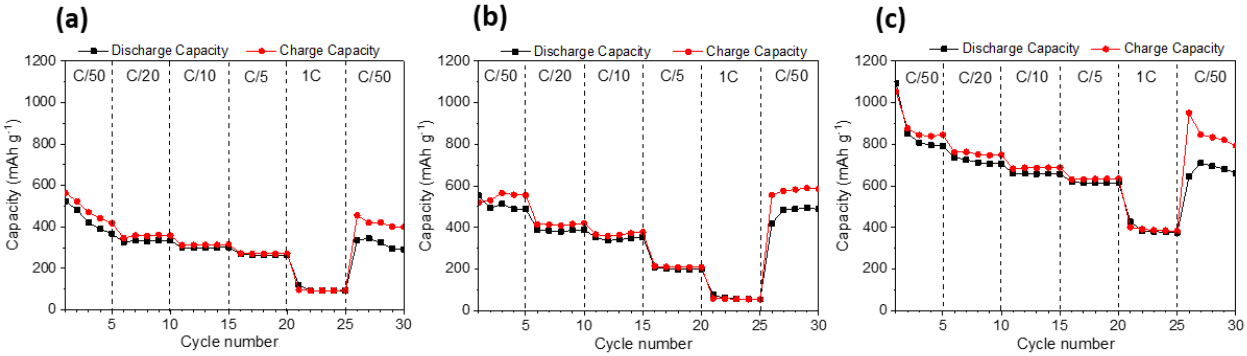

Figure 3. Rate capabilities of the (a) PVdF, (b) CMC and (c) PDDA electrodes for C-rates ranging from C/50 to 1C.

3.3. Electrochemical dilatometry

Fig. 4a-c shows the relative change of the sulfur electrode thickness along with the electrode potential during the first 2 cycles for the PVdF, CMC and PDDA formulations. The dilatometry cell was let to open circuit potential (OCP) for a period of 10 hours at the

beginning of each experiment in order to allow all the electrolyte to completely soak the thick glass frit separator. The initial OCP of the cells is about 2.9±0.1 V. The OCP of the PVdF and CMC electrodes decreases with time whereas it is stable for the PDDA electrode. The decrease in potential can be related to self-discharge process, the active material gradually dissolving and migrating to the anode due to the concentration gradient and then reacting with lithium metal, followed by conversion into polysulfides [2]. This gradual loss of active material induces a progressive decrease in the electrode thickness that reaches 5-10% after 10 hrs of OCP period for the PVdF and CMC electrodes compared to only 1.5% for the PDDA electrode. This means a reduced dissolution rate of sulfur particles for the PDDA electrode, which could be a result of a better covering of the sulfur particles by the PDDA-TFSI binder. The 1st discharge capacity is close to the coin cell value even with the large polarization of the cell, linked to the increased internal resistance in the dilatometric cell induced by the thick glass frit separator, whereas the 1st charge and the subsequent cycle show very poor cycling performance. This is attributed to the dilution of polysulfide species into the large amount of electrolyte in the thick glass frit separator, preventing further reactions due to some diffusion limitation. Indeed, when the dilatometry cell was dismantled, the separator appeared dark-orange colored, which is characteristic of the presence of a high concentration of polysulfide species. The poor cyclability in the dilatometric cell could also be caused by the smaller pressure applied on the sulfur electrode compared to a coin cell, accentuating the mechanical/electrical disconnections associated with the morphological change of the electrode.

The dilatometric curves show that in all cases most of the electrode thickness variation occurs only during the 1st plateau of the 1st discharge, in relation with the electrochemical dissolution of sulfur. When comparing the average thickness drop during the sulfur dissolution (OCP and 1st discharge plateau periods) of each formulation, it can be seen that

the PVdF electrode shows the most important collapse with a 31±6% thickness decrease, the CMC electrode displays a reduced collapse of around 22±4%, while the PDDA electrode shows an even more reduced thickness drop of around 16±3%. These values were averaged from at least 3 experiments per formulation. These results suggest that the structural integrity of the electrode is better preserved in the order of PDDA > CMC > PVdF.

Additionally, whatever the binder, there is no significant electrode thickness variation during the Li_2S deposition at the end of the 1st discharge and during the reformation of sulfur at the end of the 1st charge as well as during the subsequent sulfur dissolution/deposition cycle. Despite the fact that this behavior is impacted by the poor cyclability of the dilatometric cell, this suggests that the volume contraction of the electrode occurring during the initial sulfur dissolution is irreversible and that the volume expansion related to the formation of Li_2S and sulfur redeposition could be buffered by the large pores (sulfur depleted zones) formed in the electrodes as seen from SEM observations after the 1st discharge plateau [17]. This differs from the electrochemical dilatometry response of a binder-free Li_2S/carbon cloth (~500 μm thick) electrode, showing a reversible thickness expansion/contraction upon successive cycling [20]. This reversible dimensional change was very low in amplitude (~0.5%) and mainly related to the reversible capacitive lithiation of the carbon cloth. However, some irreversible contraction of the electrode related to the continuous dissolution of polysulfides into the electrolyte during cycling was also observed.

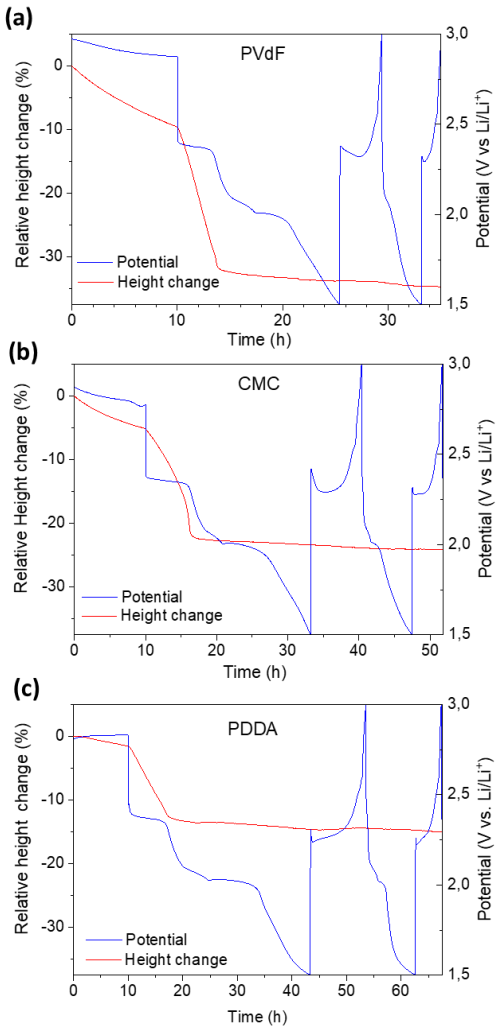

Figure 4. Evolution of the electrode thickness change and potential during the two first cycles at C/50 for the (a) PVdF, (b) CMC and (c) PDDA electrodes.

3.4. Electrochemical acoustic emission

Fig. 5a-c shows the evolution of the cumulated acoustic activity (*i.e.* number of detected AE signals per mg of sulfur in the electrode) along with the electrode potential during the first 2 cycles for the three electrode formulations. In all cases, the signals recorded display similar properties, *i.e.* a peak frequency around 300 kHz, and an amplitude between 30 and 40 dB (not shown). Such AE characteristics are typical of mechanical stress generated by the rupture of a material [37–39]. An important amount of acoustic signals is detected during the 1st plateau of the 1st discharge, when the elemental sulfur is reduced in soluble species. This acoustic activity is attributed to the relaxing of the mechanical stress resulting from the

rupture/collapse of the binder/carbon/sulfur network [17]. Hence, the binder nature and mechanical properties should have a major impact on the amount of acoustic signals measured during the 1st discharge plateau. Indeed, as seen in **Fig. 5a-c**, the average amount of acoustic hits detected during the 1st discharge plateau for PVdF and CMC formulations ranges between 4 to 5 hits mg^{-1}, while this value is decreased to 2.7 hits mg^{-1} for the PDDA electrode, meaning reduced constraints in the binder/carbon/sulfur network. Moreover, in the case of the PDDA electrode, no acoustic activity is detected after the 1st plateau, whereas some AE activity was detected during the reformation of sulfur into the collapsed electrode at the end of the charge in the case of the PVdF and CMC electrodes. This can be another consequence of the reduced mechanical constraints in the PDDA electrode compared to the other two formulations.

The AE activity detected during the 1st discharge is hence highly reminiscent of the dilatometry measurements, as the thickness drop was measured during the same period. Hence, this strongly confirms that the acoustic activity is indeed mainly linked to the electrode collapsing, leading to the height variation. The results from both techniques thus appear to follow the same trend. The PDDA electrode exhibits a smaller thickness contraction (**Fig. 4**) and a lower AE activity (**Fig. 5**) than the PVdF and CMC electrodes, which suggests a better preservation of the electrode architecture upon cycling with the PDDA binder. For further confirmation, direct observation via *in situ* synchrotron X-ray tomography was performed on the CMC and PDDA electrodes as shown below.

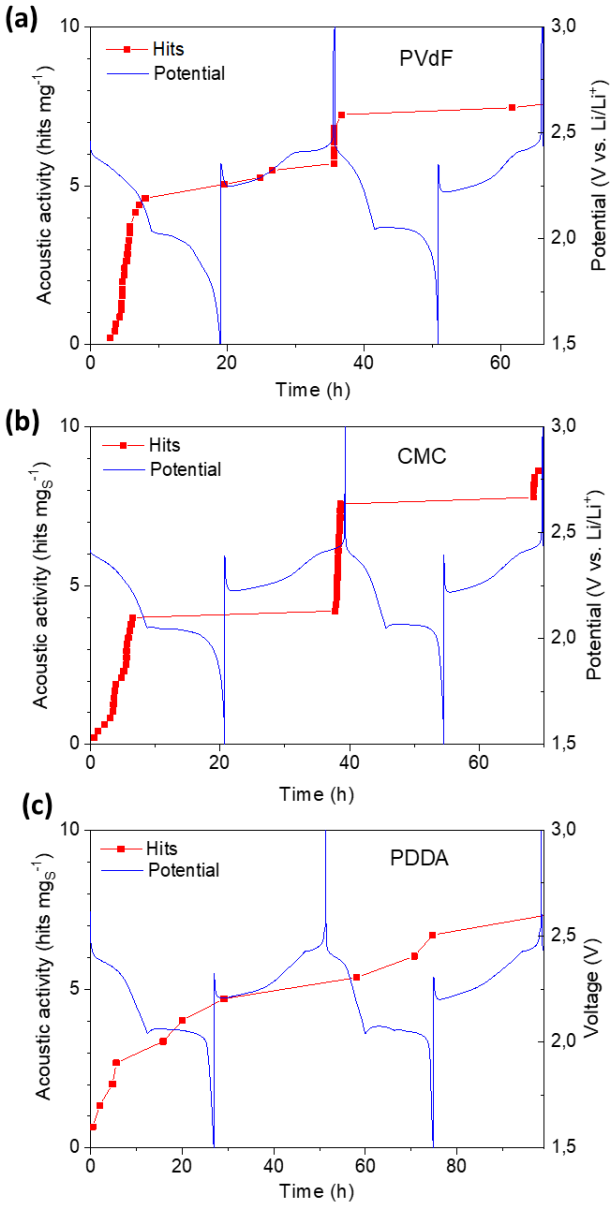

Figure 5. Evolution of the cumulated acoustic activity and potential during the first two cycles at C/50 for the (a) PVdF, (b) CMC and (c) PDDA electrodes.

3.5. In situ synchrotron X-ray tomography

The present *in situ* XRCT analyses are focused on the 1st discharge of the CMC and PDDA electrodes, *i.e.* when significant and irreversible electrode morphological changes occur as suggested from the previous electrochemical dilatometry and AE measurements. Note that coupled *in situ* synchrotron X-ray diffraction and tomography analyses performed on PDDA electrodes during complete 1st and 11th cycles are presented elsewhere [28]. XRCT

movies showing the evolution of lateral and transversal views of the CMC and PDDA electrodes during their 1st discharge are respectively shown in **Videos S1** and **S2** in supporting information. A progressive dissolution of the sulfur phase (in white) is clearly visible on the videos. However, both electrodes show an electrochemically inactive zone (remaining in white at the end of the discharge), which was already observed and discussed in our previous work [28]. It is believed to mainly originate from an insufficient and/or inhomogeneous compression of the synchrotron cell, resulting in an imperfect contact of the electrode on the current collector. Consequently, the 1st discharge capacity of both electrodes in the XRCT cell is lower than measured in coin cell and dilatometric cell, with a 1st discharge capacity of about 340 and 660 mAh g^{-1} for the CMC and PDDA electrode, respectively (see their discharge voltage profile during XRCT in **Fig. S2** in supporting information). However, by focusing on the electroactive area of the electrodes, relevant information on their morphological changes can be extracted nevertheless.

Fig. 6 shows cross-sectional XRCT views in the electroactive areas of the CMC and PDDA electrodes at different steps of the 1st discharge, namely at the initial state (0% depth-of-discharge (DOD)), at half of discharge (50% DOD) and at the end of discharge (100% DOD). In both systems, at least four phases can be identified on the images: *(i)* the separator fibers in a dark gray level (here appearing through cross-sectional round shapes); *(ii)* the large sulfur particle clusters in white; *(iii)* a sulfur-rich phase in light gray, containing lower diameter sulfur particles not distinguishable from the binder and carbon black due to spatial resolution limitations, and *(iv)* a porous sulfur-free phase in mid-tone gray, filled with electrolyte and also containing the undiscernible binder and carbon black.

At 0% of DOD of both electrodes, it can be seen that most of the imaged electrode is filled with the sulfur phase. One can also note that the S particles/clusters are more clearly discernible in the CMC electrodes, suggesting their higher agglomeration than in the PDDA

electrode, in accordance with the previous SEM observations. At 50% of DOD, in both cases, it appears that most of the sulfur phase has been dissolved, leaving the porous carbon-binder domain (CBD) phase filled with electrolyte. Additionally, black zones of several μm in size can be observed in the CMC electrode. Their black color indicates that their X-ray attenuation coefficient is very low and thus suggests the formation of gas-filled pores. However, considering that the sulfur dissolution process requires the presence of electrolyte and does not involve the production of gas, the formation of holes without electrolyte in some sulfur-depleted zones of the CMC electrode is very surprising and inexplicable. Further XRCT analyses will be required to confirm/elucidate this observation. No Li_2S and/or Li_2S_2 solid phase can be observed at the end of the discharge (100% DOD) in either electrode. This can be a consequence of their nanometer size making them not discernible on the tomography images due to resolution limitations and have not yet been observed by XRCT in the literature [25–28].

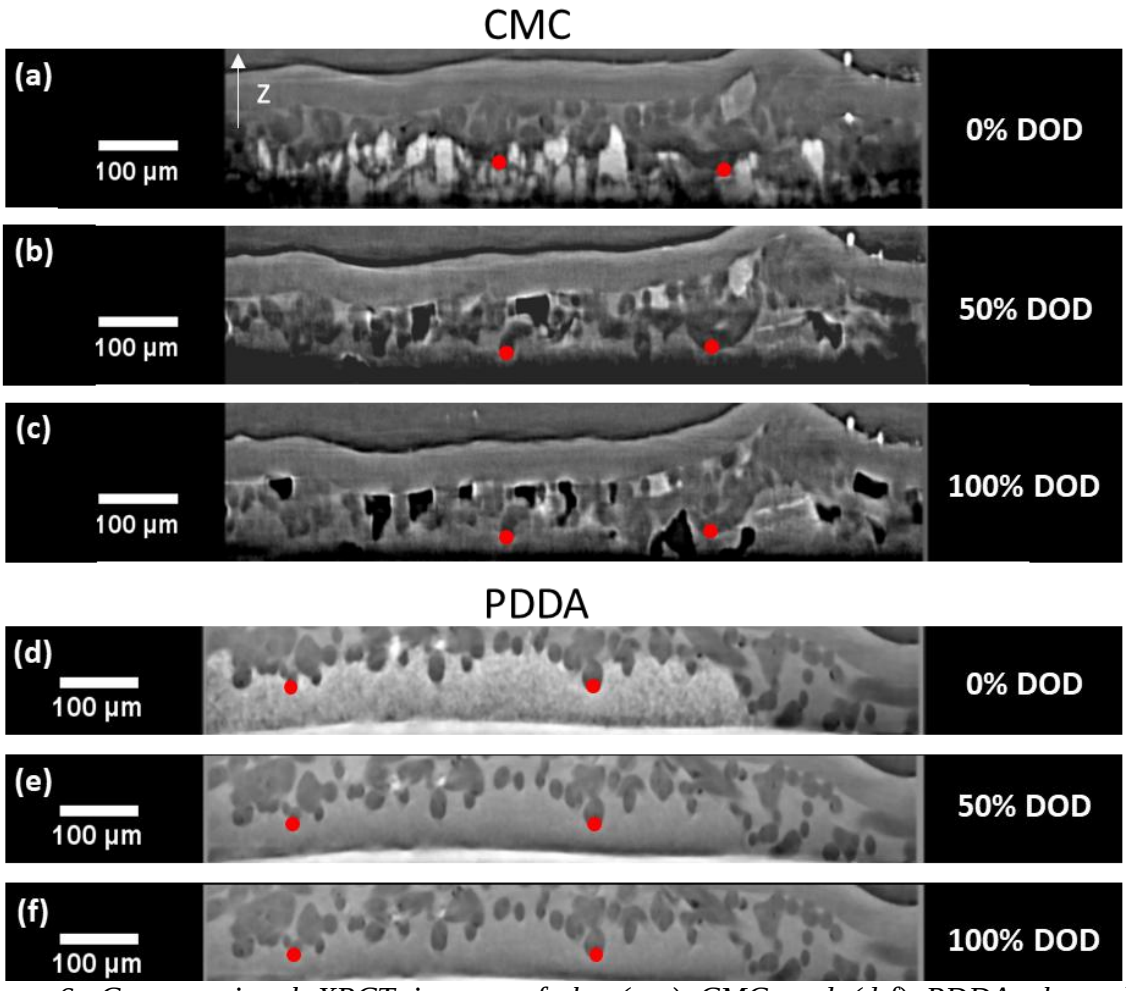

Figure 6. Cross-sectional XRCT images of the (a-c) CMC and (d-f) PDDA electrodes acquired at different stages (0, 50 and 100% DOD) of the 1st discharge. The red dots correspond to selected separator fiber positions for measuring the electrode thickness variation.

In order to confirm the dilatometry measurements, the thickness variation of the CMC and PDDA electrodes was quantified from the tomography images by selecting five separator fibers across the electrochemically active areas of the cells (some of those fibers are marked with a red dot in **Fig. 6**) and measuring their distance to the aluminum current collector, thus giving a representation of the thickness of the sulfur electrode at each acquisition step. On the basis of these analyses, the relative average thickness variation of the CMC and PDDA electrodes can be quantified and is shown in **Fig. 7** as a function of the sulfur consumption in %, which is determined from segmentation of the sulfur phase in the reconstructed electrode volume. During the first 50-60% of sulfur dissolution, both electrode follow a constant and

relatively similar thickness decrease. However, after around 60% of sulfur dissolution, the thickness of the CMC electrode drops with a much faster slope, before stabilizing during the last 10% of the dissolution process, while the decrease of the PDDA electrode remains globally constant. Thus, at the end of the sulfur consumption, the total thickness decrease of the CMC electrode ends around ~24%, *versus* ~12% for the PDDA electrode. The difference in the final irreversible thickness contraction of the electrode between these two binder formulations is in accordance with the dilatometry data.

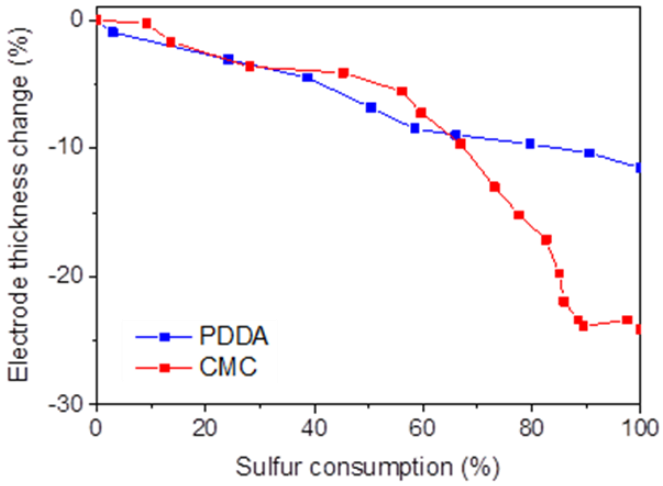

Figure 7. Relative variation of the CMC and PDDA electrode thickness as a function of the sulfur consumption rate during the 1st discharge determined from in situ XRCT analyses.

This different behavior of each electrode observed in **Fig. 7** can be attributed to the specific properties of each binder. During the initial stage of the discharge, the diameter of the larger sulfur particles is reduced, and the smaller particles are fully dissolved [28]. Both CMC and PDDA binders can accommodate this morphological evolution thanks to their softness, and thus a continuous decrease of the electrode thickness is observed. Further down the discharge process, the larger particles get completely dissolved and the elasticity of the CMC network is not sufficient to maintain the mechanical integrity of the electrode, resulting in its collapse and thus a fast drop in the electrode thickness is observed. On the other hand, the PDDA based electrode shows a more linear thickness evolution throughout all the sulfur consumption, suggesting a higher mechanical strength of the PDDA-TFSI network. To the

best of our knowledge, there is no literature data about the mechanical properties of PDDA-TFSI, but a possible explanation is that the ability of the polysulfide dianions to bind to the cationic pyrrolidinium moieties of the PDDA-TFSI binder [14] could create a cross-linked polymer network formed by ionic interactions, improving the electrode stability through cycling. Moreover, assuming a better dispersion degree of the ink with the PDDA binder as previously argued, a better developed and homogeneous network of S/CB/binder is likely to be generated in the dried electrode, resulting in a higher mechanical strength of the PDDA electrode.

4. Conclusions

In this study, the morphological degradation with cycling of sulfur-based electrodes using a PDDA-TFSI polyelectrolyte binder was characterized and compared to those of more conventional PVdF and CMC binders. Electrochemical dilatometry was used for one of the first times on the Li/S system in order to measure the sulfur electrode collapse during the first discharge. This pointed out that the PDDA-based electrode showed reduced irreversible thickness variation compared to CMC and PVdF binders, which was then confirmed by measuring the electrode thickness variation on XRCT images of both PDDA-TFSI and CMC-based electrodes. On top of those results, the polyelectrolyte-based electrode also displayed a much reduced acoustic activity measured *via operando* AE compared to the other two electrode formulations, which was associated with a lower mechanical stress resulting from the rupture of the binder/carbon/sulfur network. All these results point out that the excellent electrochemical performance of the PDDA-TFSI based electrode is not only linked to its polysulfide-confining properties but also to an improved morphological stability of the overall electrode. These conclusions add further interest to multifunctional binders combining polysulfide-regulating abilities as well as enhanced mechanical properties, and

polyelectrolyte binders in particular stand as promising candidates for further studies and potential industrialization.

Supporting Information

Schematics of the dilatometry, acoustic emission and XRCT electrochemical cells, voltage profiles of the CMC and PDDA electrodes during the 1st discharge in the XRCT cell, videos of lateral and transversal XRCT images of the CMC and PDDA electrodes during the 1st discharge.

Acknowledgements

The authors thank the Natural Sciences and Engineering Research Council (NSERC) of Canada (Grant No. RGPIN-2016-04524), the "Fonds de recherche du Québec – Nature et technologies" (FRQ-NT, grant No. 2018-PR-205823) and the Auvergne Rhône-Alpes region (ADR ARC 2016 N°16-005614-01) for supporting this work. We also thank the ESRF and SOLEIL synchrotrons' reviewing committees for shifts allocation and the beamline scientists of ID11 and Psiché, M. Majkut, J. Wright, C. Nemoz and A. King. The author gives a special thought to V. Vanpeene, D. Devaux, L. Magnier and Q. Saby for their precious help and support during the *in situ* XRCT experiments.

References

[1] P.G. Bruce, S.A. Freunberger, L.J. Hardwick, J.-M. Tarascon, Li–O_2 and Li–S batteries with high energy storage, Nature Materials. 11 (2012) 19–29. https://doi.org/10.1038/nmat3191.

[2] A. Manthiram, Y. Fu, S.-H. Chung, C. Zu, Y.-S. Su, Rechargeable Lithium–Sulfur Batteries, Chem. Rev. 114 (2014) 11751–11787. https://doi.org/10.1021/cr500062v.

[3] R. Kumar, J. Liu, J.-Y. Hwang, Y.-K. Sun, Recent research trends in Li–S batteries, J. Mater. Chem. A. 6 (2018) 11582–11605. https://doi.org/10.1039/C8TA01483C.

[4] M.A. Pope, I.A. Aksay, Structural Design of Cathodes for Li-S Batteries, Advanced Energy Materials. 5 (2015) 1500124. https://doi.org/10.1002/aenm.201500124.

[5] Q. Guo, Z. Zheng, Rational Design of Binders for Stable Li-S and Na-S Batteries, Advanced Functional Materials. 30 (2020) 1907931. https://doi.org/10.1002/adfm.201907931.

[6] C. Barchasz, J.-C. Leprêtre, F. Alloin, S. Patoux, New insights into the limiting parameters of the Li/S rechargeable cell, Journal of Power Sources. 199 (2012) 322–330. https://doi.org/10.1016/j.jpowsour.2011.07.021.

[7] M.J. Lacey, F. Jeschull, K. Edström, D. Brandell, Why PEO as a binder or polymer coating increases capacity in the Li–S system, Chem. Commun. 49 (2013) 8531–8533. https://doi.org/10.1039/C3CC44772C.

[8] M. He, L.-X. Yuan, W.-X. Zhang, X.-L. Hu, Y.-H. Huang, Enhanced Cyclability for Sulfur Cathode Achieved by a Water-Soluble Binder, (2011). https://doi.org/10.1021/jp2043416.

[9] Z. Zhang, W. Bao, H. Lu, M. Jia, K. Xie, Y. Lai, J. Li, Water-Soluble Polyacrylic Acid as a Binder for Sulfur Cathode in Lithium-Sulfur Battery, ECS Electrochem. Lett. 1 (2012) A34–A37. https://doi.org/10.1149/2.009202eel.

[10] Q. Pang, X. Liang, C.Y. Kwok, J. Kulisch, L.F. Nazar, A Comprehensive Approach toward Stable Lithium–Sulfur Batteries with High Volumetric Energy Density, Advanced Energy Materials. 7 (2017) 1601630. https://doi.org/10.1002/aenm.201601630.

[11] W. Li, Q. Zhang, G. Zheng, Z.W. Seh, H. Yao, Y. Cui, Understanding the Role of Different Conductive Polymers in Improving the Nanostructured Sulfur Cathode Performance, Nano Lett. 13 (2013) 5534–5540. https://doi.org/10.1021/nl403130h.

[12] G. Ai, Y. Dai, Y. Ye, W. Mao, Z. Wang, H. Zhao, Y. Chen, J. Zhu, Y. Fu, V. Battaglia, J. Guo, V. Srinivasan, G. Liu, Investigation of surface effects through the application of the functional binders in lithium sulfur batteries, Nano Energy. 16 (2015) 28–37. https://doi.org/10.1016/j.nanoen.2015.05.036.

[13] H. Su, C. Fu, Y. Zhao, D. Long, L. Ling, B.M. Wong, J. Lu, J. Guo, Polycation Binders: An Effective Approach toward Lithium Polysulfide Sequestration in Li–S Batteries, ACS Energy Lett. 2 (2017) 2591–2597. https://doi.org/10.1021/acsenergylett.7b00779.

[14] L. Li, T.A. Pascal, J.G. Connell, F.Y. Fan, S.M. Meckler, L. Ma, Y.-M. Chiang, D. Prendergast, B.A. Helms, Molecular understanding of polyelectrolyte binders that actively regulate ion transport in sulfur cathodes, Nat Commun. 8 (2017) 1–10. https://doi.org/10.1038/s41467-017-02410-6.

[15] A. Etiemble, H. Idrissi, L. Roué, On the decrepitation mechanism of MgNi and LaNi5-based electrodes studied by in situ acoustic emission, Journal of Power Sources. 196 (2011) 5168–5173. https://doi.org/10.1016/j.jpowsour.2011.01.098.

[16] A. Tranchot, A. Etiemble, P.-X. Thivel, H. Idrissi, L. Roué, In-situ acoustic emission study of Si-based electrodes for Li-ion batteries, Journal of Power Sources. 279 (2015) 259–266. https://doi.org/10.1016/j.jpowsour.2014.12.126.

[17] Q. Lemarié, F. Alloin, P.X. Thivel, H. Idrissi, L. Roué, Study of sulfur-based electrodes by operando acoustic emission, Electrochimica Acta. 299 (2019) 415–422. https://doi.org/10.1016/j.electacta.2019.01.019.

[18] M. Bauer, M. Wachtler, H. Stöwe, J.V. Persson, M.A. Danzer, Understanding the dilation and dilation relaxation behavior of graphite-based lithium-ion cells, Journal of Power Sources. 317 (2016) 93–102. https://doi.org/10.1016/j.jpowsour.2016.03.078.

[19] A. Tranchot, H. Idrissi, P.X. Thivel, L. Roué, Impact of the slurry pH on the expansion/contraction behavior of silicon/carbon/carboxymethylcellulose electrodes for li-ion batteries, Journal of the Electrochemical Society. 163 (2016) undefined-undefined. https://doi.org/10.1149/2.1071606jes.

[20] M. Li, Z. Wang, E. Detsi, In Situ Electrochemical Dilatometry Study of (De)lithiation and Polysulfide Dissolution-Induced Dimensional Changes in Lithium-Sulfur Cathodes during Charging and Discharging, J. Electrochem. Soc. 167 (2020) 050505. https://doi.org/10.1149/1945-7111/ab63c1.

[21] D. P. Finegan, M. Scheel, J. B. Robinson, B. Tjaden, M.D. Michiel, G. Hinds, D.J. L. Brett, P. R. Shearing, Investigating lithium-ion battery materials during overcharge-induced thermal runaway: an operando and multi-scale X-ray CT study, Physical Chemistry Chemical Physics. 18 (2016) 30912–30919. https://doi.org/10.1039/C6CP04251A.

[22] V. Vanpeene, A. King, E. Maire, L. Roué, In situ characterization of Si-based anodes by coupling synchrotron X-ray tomography and diffraction, Nano Energy. 56 (2019) 799–812. https://doi.org/10.1016/j.nanoen.2018.11.079.

[23] V. Vanpeene, J. Villanova, A. King, B. Lestriez, E. Maire, L. Roué, Dynamics of the Morphological Degradation of Si-Based Anodes for Li-Ion Batteries Characterized by

In Situ Synchrotron X-Ray Tomography, Advanced Energy Materials. 9 (2019) 1803947. https://doi.org/10.1002/aenm.201803947.

[24] D.S. Eastwood, P.M. Bayley, H.J. Chang, O.O. Taiwo, J. Vila-Comamala, D.J.L. Brett, C. Rau, P.J. Withers, P.R. Shearing, C.P. Grey, P.D. Lee, Three-dimensional characterization of electrodeposited lithium microstructures using synchrotron X-ray phase contrast imaging, Chem. Commun. 51 (2014) 266–268. https://doi.org/10.1039/C4CC03187C.

[25] A. Yermukhambetova, C. Tan, S.R. Daemi, Z. Bakenov, J.A. Darr, D.J.L. Brett, P.R. Shearing, Exploring 3D microstructural evolution in Li-Sulfur battery electrodes using *in-situ* X-ray tomography, Scientific Reports. 6 (2016) 35291. https://doi.org/10.1038/srep35291.

[26] L. Zielke, C. Barchasz, S. Waluś, F. Alloin, J.-C. Leprêtre, A. Spettl, V. Schmidt, A. Hilger, I. Manke, J. Banhart, R. Zengerle, S. Thiele, Degradation of Li/S Battery Electrodes On 3D Current Collectors Studied Using X-ray Phase Contrast Tomography, Scientific Reports. 5 (2015) 10921. https://doi.org/10.1038/srep10921.

[27] G. Tonin, G. Vaughan, R. Bouchet, F. Alloin, M.D. Michiel, L. Boutafa, J.-F. Colin, C. Barchasz, Multiscale characterization of a lithium/sulfur battery by coupling operando X-ray tomography and spatially-resolved diffraction, Scientific Reports. 7 (2017) 2755. https://doi.org/10.1038/s41598-017-03004-4.

[28] Q. Lemarié, E. Maire, H. Idrissi, P.-X. Thivel, F. Alloin, L. Roué, Sulfur-Based Electrode Using a Polyelectrolyte Binder Studied via Coupled in Situ Synchrotron X-ray Diffraction and Tomography, ACS Appl. Energy Mater. (2020). https://doi.org/10.1021/acsaem.9b02108.

[29] A. Mirone, E. Brun, E. Gouillart, P. Tafforeau, J. Kieffer, The PyHST2 hybrid distributed code for high speed tomographic reconstruction with iterative reconstruction

and a priori knowledge capabilities, Nuclear Instruments and Methods in Physics Research Section B: Beam Interactions with Materials and Atoms. 324 (2014) 41–48. https://doi.org/10.1016/j.nimb.2013.09.030.

[30] J. Schindelin, I. Arganda-Carreras, E. Frise, V. Kaynig, M. Longair, T. Pietzsch, S. Preibisch, C. Rueden, S. Saalfeld, B. Schmid, J.-Y. Tinevez, D.J. White, V. Hartenstein, K. Eliceiri, P. Tomancak, A. Cardona, Fiji: an open-source platform for biological-image analysis, Nat. Methods. 9 (2012) 676–682. https://doi.org/10.1038/nmeth.2019.

[31] X. Hong, J. Jin, Z. Wen, S. Zhang, Q. Wang, C. Shen, K. Rui, On the dispersion of lithium-sulfur battery cathode materials effected by electrostatic and stereo-chemical factors of binders, Journal of Power Sources. 324 (2016) 455–461. https://doi.org/10.1016/j.jpowsour.2016.04.114.

[32] S. Waluś, A. Robba, R. Bouchet, C. Barchasz, F. Alloin, Influence of the binder and preparation process on the positive electrode electrochemical response and Li/S system performances, Electrochimica Acta. 210 (2016) 492–501. https://doi.org/10.1016/j.electacta.2016.05.130.

[33] C. Barchasz, F. Molton, C. Duboc, J.-C. Leprêtre, S. Patoux, F. Alloin, Lithium/Sulfur Cell Discharge Mechanism: An Original Approach for Intermediate Species Identification, Anal. Chem. 84 (2012) 3973–3980. https://doi.org/10.1021/ac2032244.

[34] X.-B. Cheng, R. Zhang, C.-Z. Zhao, Q. Zhang, Toward Safe Lithium Metal Anode in Rechargeable Batteries: A Review, Chem. Rev. 117 (2017) 10403–10473. https://doi.org/10.1021/acs.chemrev.7b00115.

[35] X.-B. Cheng, J.-Q. Huang, Q. Zhang, Review—Li Metal Anode in Working Lithium-Sulfur Batteries, J. Electrochem. Soc. 165 (2017) A6058. https://doi.org/10.1149/2.0111801jes.

[36] D. Lin, Y. Liu, Y. Cui, Reviving the lithium metal anode for high-energy batteries, Nature Nanotechnology. 12 (2017) 194–206. https://doi.org/10.1038/nnano.2017.16.

[37] Z. Nazarchuk, V. Skalskyi, O. Serhiyenko, Acoustic Emission: Methodology and Application, Springer International Publishing, 2017. https://doi.org/10.1007/978-3-319-49350-3.

[38] G. Romhány, T. Czigány, J. Karger-Kocsis, Failure Assessment and Evaluation of Damage Development and Crack Growth in Polymer Composites Via Localization of Acoustic Emission Events: A Review, J Macromol Sci Phys. 57 (2017) 397–439. https://doi.org/10.1080/15583724.2017.1309663.

[39] I.M. De Rosa, C. Santulli, F. Sarasini, Acoustic emission for monitoring the mechanical behaviour of natural fibre composites: A literature review, Composites Part A: Applied Science and Manufacturing. 40 (2009) 1456–1469. https://doi.org/10.1016/j.compositesa.2009.04.030.